The chemical throwing power of lithium-based inhibitors from organic coatings on AA2024-T3

Visser, P.; Marcoen, K.; Trindade, G. F.; Abel, M. L.; Watts, J. F.; Hauffman, T.; Mol, J. M.C.; Terryn, H.

Important note
To cite this publication, please use the final published version (if applicable).
Please check the document version above.

The chemical throwing power of lithium-based inhibitors from organic coatings on AA2024-T3

P. Visser[a,b,*], K. Marcoen[c], G.F. Trindade[d,1], M-L. Abel[d], J.F. Watts[d], T. Hauffman[c], J.M.C. Mol[a], H. Terryn[a,c]

[a] Delft University of Technology, Department of Materials Science and Engineering, Mekelweg 2, 2628 CD, Delft, the Netherlands
[b] AkzoNobel, Rijksstraatweg 31, 2171 AJ, Sassenheim, the Netherlands
[c] Vrije Universiteit Brussel, Research Group of Electrochemical and Surface Engineering (SURF), Pleinlaan 2, 1050, Brussels, Belgium
[d] The Surface Analysis Laboratory, Department of Mechanical Engineering Sciences, University of Surrey, Guildford, Surrey, GU2 7XH, UK

ABSTRACT

Chemical throwing power, being the distance over which an inhibitor is able to protect a defect effectively, is an important parameter for active protective coatings. This study investigates the chemical throwing power of lithium-based leachable corrosion inhibitors exhibiting different leaching kinetics, from coatings at different inhibitor loading concentrations. The results demonstrate that Li-salt loaded coatings provide corrosion protection of defect areas up to a width of 6 mm. Time-of-flight secondary ion mass spectrometry (ToF-SIMS) was used to detect the lateral spread of Li in the defect areas and provide the chemical speciation of corrosion protective layers in the defect areas.

1. Introduction

Traditionally, active protective coatings have typically two functionalities. Firstly, the coating provides barrier properties and secondly, active corrosion protection can be achieved by the ability to release corrosion inhibitors from the coating matrix into in a defect area in case the coating is damaged. Leaching of the inhibitor is the complex process where condensed moisture diffuses into the coating matrix and triggers the dissolution of the corrosion inhibitor and facilitates the transport of the corrosion inhibitive species from the coating matrix to the exposed substrate [1]. The release kinetics and the capacity of the reservoir of corrosion inhibitor in the coating are essential parameters to consider for such active protective systems [2,3]. The inhibitor release kinetics are affected by the solubility of the corrosion inhibitor, the loading in the coating, and the microstructure of the coating matrix [4]. Several studies have been performed on the leaching behaviour of chromate inhibitors, which have been the industry standard for an effective active corrosion protection for many decades [5–10]. In these studies it was found that the inhibitor release does not occur via diffusion through the resin of the coating itself and is not controlled by a Fickian diffusion process either [5,6]. Instead, the inhibitor is released due to the direct dissolution of clusters of inhibitors, which are in contact with the electrolyte at the surface of the coating or at the defect area [8]. After

this initial fast inhibitor release, the process continues via diffusion through a fractional network of voids and inter-connected pathways deeper in the coating matrix left after the prior dissolution of the corrosion inhibitor, resulting in a slower inhibitor release over time [8,9]. This knowledge has been modelled to further understand the mechanism of inhibitor transport in coatings [6,7].

Another important parameter is the distance over which the coating is able to protect a defect effectively, known as the "throwing power" [11,12]. The ability of a coating to provide corrosion protection of a defect by the release of inhibitors can be classified as the "chemical" throwing power, this process involves a concentration gradient-driven random transport from inhibitor-rich regions (coating) to unprotected sites (defect) [13]. Scully and Presuel-Moreno studied the phenomenon of chemical throwing power in addition with the galvanic throwing power using an Al-Co-Ce metallic coating over AA2024-T351 under thin electrolyte films representative of atmospheric conditions and demonstrated the effect of defect size, showing that the larger the scratch size, the more difficult it is to transport sufficient inhibitor to the centre-line of the defect and suppress corrosion [12,14]. In addition to the galvanic protection mechanism, the conditions for the chemical throwing power under which Al-Co-Ce coatings released and transported Ce³⁺ ions to a defect on AA2024-T351 was investigated. One of the key criteria to obtain effective inhibition by was the ability to
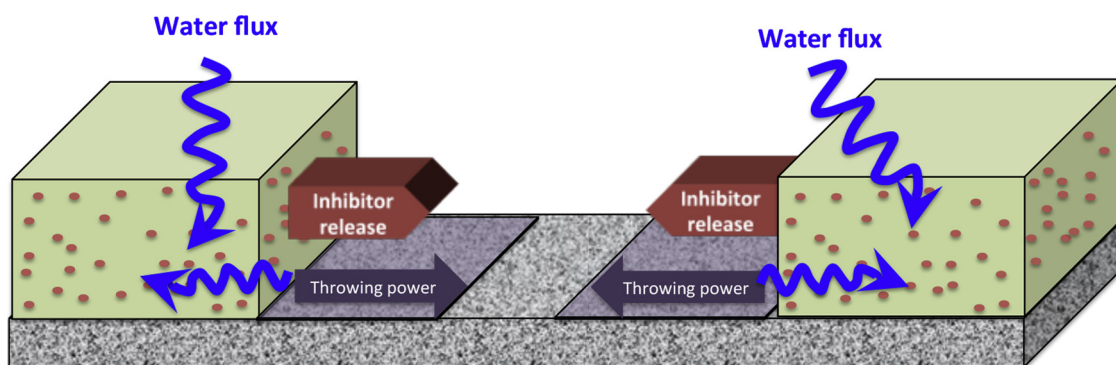
Fig. 1. The concept of chemical throwing power by active corrosion protective coatings.

achieve a critical inhibitor concentration in the defect within a few hours. It was demonstrated that such Al-Co-Ce coatings could be tailored to optimize coating functionality by a combination of galvanic and chemical inhibition properties.

The concept of chemical throwing power can also be projected on the concept of active corrosion protection from coatings with an organic matrix. Fig. 1 shows the concept of chemical throwing power as the lateral spread of a corrosion protective layer in a defect as a result of the release of corrosion inhibiting species from a coating matrix through leaching. Inhibitor leaching is triggered by water ingress through the top-surface and the cut-edge of the coating to provide active protection in the defect area. In addition to parameters such as inhibitor leach-rate and permeability of the coating matrix are key criteria to obtain the critical inhibitor concentration. In addition to this, the irreversibility or stability of the developed passive layer in the defect is an other important aspect to obtain effective active corrosion protection [13,15].

In 2010, Li-salts were introduced as leachable corrosion inhibitor in active protective coatings for the protection of aluminium alloys [16]. Several studies have demonstrated that Li-leaching coatings provide fast, effective and irreversible corrosion protection in a coating defect and the technology is regarded as a promising environmentally friendly alternative to the toxic chromates [17–19]. The active protective properties of these coatings are obtained by the leaching of Li-salts from the organic coating matrix, this release of the Li-salts provides favourable alkaline conditions in the defect area which facilitates the formation of a protective aluminium oxide/hydroxide layer in the defect area [20,21]. The protective layer comprises mainly aluminium, oxygen and lithium and electrochemical studies revealed that the corrosion protective properties of the layer could be linked to the dense layer at the aluminium substrate [20,22]. Further investigations showed that the protective layer in the defects featured different surface morphologies which indicates possible different compositions as a consequence of different Li concentrations and pH during the formation of the layer [23,24]. Marcoen et al. used the high sensitivity towards Li and the high lateral resolution of time-of-flight secondary ion mass spectrometry (ToF-SIMS) to investigate the Li-spread in a 1 mm wide defect area and unravelled the surface composition of the protective layers [25]. It was found that the Li-spread in a 1 mm wide defect area was relatively fast and the entire defect area was covered with Li-based species within 15 min of exposure in the neutral salt spray test (NSS). Short exposures to these corrosive conditions induced the formation of a Li-containing pseudoboehmite (Li-PB) and longer exposure times resulted in higher Li-concentrations in the defect area and the formation of a Li-based layered double hydroxide (Li-LDH) covering the entire surface area. However, the chemical throwing power of Li-salts as corrosion inhibitor by leaching from organic coatings has not been studied yet.

This paper presents the study of the chemical throwing power of Li-salts, i.e. lithium carbonate and lithium oxalate, when incorporated into organic coatings as leachable corrosion inhibitor. Firstly, the leaching characteristics and the corrosion protective properties of organic coatings with high and low loadings of Li-salts were investigated. Then, the chemical throwing power was assessed by exposing these coatings with increasing defect widths up to 6 mm to neutral salt spray conditions for 7 days. The corrosion protective performance of the systems was assessed optically and by using profilometry. In addition, ToF-SIMS was used to investigate the lateral Li-spread and the surface composition of the protective layer in the defect areas. This study provides a further understanding of the active corrosion protective properties, the surface composition of the protective layer in the defect area and demonstrates the "chemical" throwing power of the Li-salt based inhibitor leaching technology, a feature that has not been demonstrated for any other chromate-free inhibitor leaching coating technology.

2. Experimental

2.1. Materials and sample preparation

2.1.1. Inhibitor loaded coatings

Polyurethane model coatings with a total pigment volume concentration (PVC) of 30% and respective loadings of 15 and 2.5% PVC Li-salt as leachable corrosion inhibitor were used in this study. The composition of the model coatings is listed in Table 1. Analytical grade lithium carbonate and lithium oxalate were acquired from Sigma-Aldrich.

2.1.2. Preparation of the organic model coatings

The Li-leaching model coatings were prepared in a similar way as described in previous papers [20,21]. Component A was prepared by the sequential addition of the raw materials to a 370 ml glass jar. After mixing the materials to a homogeneous mixture, 400 g of Zirconox pearls® (1.7–2.4 mm) were added and the samples were shaken on a

Table 1
Composition of the Li-salt loaded organic model coatings.

leachable inhibitor		lithium carbonate		lithium oxalate	
loading (PVC %)		15%	2.50%	15%	2.50%
Component A					
N-Butylacetate	Sigma Aldrich	85.0 g	85.0 g	85.0 g	85.0 g
Desmophen 650MPA	Covestro	47.7 g	47.7 g	47.7 g	47.7 g
Lithium carbonate	Sigma Aldrich	23.6 g	3.6 g	–	–
Lithium oxalate	Sigma Aldrich	–	–	23.2 g	3.6 g
Magnesium oxide	Sigma Aldrich	16.4 g	16.4 g	16.4 g	16.4 g
Tioxide TR 92	Huntsman	5.2 g	5.2 g	5.2 g	5.2 g
Blanc Fixe N (Ba (SO₄))	Sachtleben	15.4 g	58.1 g	15.4 g	58.1 g
Component B					
Tolonate HDB 75 MX	Vencorex	28.5 g	28.5 g	28.5 g	28.5 g
Dynasilan Glymo	Evonik	5.2 g	5.2 g	5.2 g	5.2 g

Skandex® paint shaker to grind and disperse the pigments to a grind fineness less than 25 μm. After this shaking procedure, the pearls were separated from the paint and Component B was added. The paint was then stirred for 5 min to a homogeneous mixture.

2.1.3. Sample preparation

Sheet material of AA2024-T3 aluminium alloy with a thickness of 0.8 mm was anodized according aerospace requirements (AIPI 02-01-003) in tartaric sulphuric acid (TSA) to obtain an anodic film with a thickness of 3–3.5 μm. The model coatings were applied using a high-volume low-pressure (HVLP) spray gun at 23 °C and 55% relative humidity. After the application, all coatings were cured with a forced cure cycle of 16 h at 80 °C after a 1 h flash-off period. All coatings had a dry film layer thickness of 20–25 μm.

2.1.4. Inhibitor leaching

Two coated panels of 7×2 cm were immersed in a plastic test tube (total sample area 28 cm^2) with 50 ml demineralized water to study the leaching behaviour of the coatings with different loading concentrations of corrosion inhibitor. After 4 h, 24 h, 72 h, 120 h and 192 h immersion the entire solution with the leached inhibitor was removed and replaced by fresh demineralized water. The removed solutions were acidified with nitric acid to a concentration of 0.1 M and analysed with inductively coupled plasma atomic emission spectroscopy (Arcos NT ICP-AES) using scandium as an internal standard. On order to compare the different coatings, the accumulated release of Li in mM/L in the water was normalized to a dry film thickness of 25 μm/cm^2. All measurements for the leaching curves were executed in triplicate.

2.1.5. Corrosion protection in the defect area

In order to assess the active protective properties of these coatings, an artificial defect consisting of two intersecting scribes with a width of 1 mm, a length of 2 cm and a depth of 100–150 μm was made in the coatings by mechanical milling. The damaged coatings were exposed to the neutral salt spray test (NSS) according to ASTM-B117 for 168 h. After the exposure the scribes were studied using microscopy and electrochemical techniques.

2.1.6. Inhibitor throwing power

Coated panels with four parallel defects with varying widths (0.5 mm, 1.5 mm, 3 mm and 6 mm) were prepared using a Gravograph® mechanical engraving machine as shown in Fig. 2. The panels were placed in the NSS cabinets at an angle of 20 degrees with a vertical positioning of the defects to assess the lateral chemical throwing power of these active corrosion inhibiting coating systems.

After 168 h NSS exposure, the scribed panels were examined with an optical microscope and the surface roughness (Sa) of the defect areas was measured with a Bruker K1 white light interferometer using a 20 X objective. The Sa value expresses the surface roughness of an area, as an absolute value, the difference in height of each point compared to the arithmetical mean of the surface. All data was analysed with the Vision for Profilers (version 4.2) software.

2.1.7. Reference samples

Reference samples were prepared for the compositional analysis of the deposites generated within the protective layer in the defect area [25]. Aluminium panels, AA2024-T3 (0.8 mm thickness), were cleaned with acetone (> 99.9%, SASOL Chemie Gmbh & Co. KG) and scribed (1 mm) as described above. Pseudoboehmite (PB) and Li-containing pseudoboehmite (Li-PB) reference samples were prepared according to the method of Gorman et al. by immersing the scribed panels in (i) demineralized water or (ii) a 0.02 M LiCl (BioXtra, ≥99.0%, Sigma–Aldrich) solution in demineralized water at 95–100 °C for 1 h to obtain PB or Li-PB respectively [26]. In addition, a Li-based layered double hydroxide (Li-LDH) reference coating was obtained by the immersion of a scribed AA2024-T3 panel in a 0.1 M Li-carbonate solution for 15 min according to the method of Buchheit et al. [27]. Following the treatment, the panels were rinsed with copious amounts of demineralized water and dried at the air. All ToF–SIMS measurements were performed in the scribed areas.

2.2. Surface analytical methods

2.2.1. Optical and scanning electron microscopy (SEM)

The defect areas were examined by optical and scanning electron microscopy techniques. The optical microscope was used to visualize the effects of the corrosive conditions in the defect areas of the coatings. A JEOL JSM-7100F field emission scanning electron microscope was used to study the surface and cross-section morphology of the corrosion inhibiting layers in the defect areas. The surface morphology investigations were performed with the secondary electron detector (SEI) using an acceleration voltage of 5 kV at a working distance of 10 mm. The cross-sectional analysis of the defect areas were performed with a backscatter electron detector (BED-C) at 5 kV and a working distance of 3 mm. Prior to the analysis of the cross-sections, the samples were sectioned with a diamond saw and the defect area was prepared with a Hitachi IM4000 ion milling system using 6 kV Ar-ion acceleration, a rotation speed of 3 rpm and a swing angle of $+/-30°$.

2.2.2. Time-of-flight secondary ion mass spectrometry (ToF-SIMS)

In order to study the Li-spread in the defect areas, ToF-SIMS measurements were performed on a TOF.SIMS 5 system (ION-TOF GmbH,
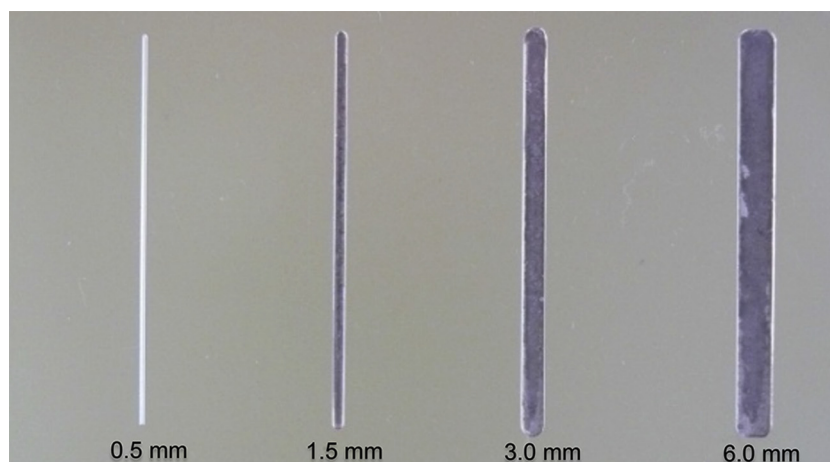

Fig. 2. Example of a coated panel with vertical scribes ranging from 0.5 mm to 6 mm in width used to assess the chemical throwing power.

Münster, Germany). Positive ion mass spectra were acquired over a mass range of 1–800 amu using a 30 keV Bi_3^+ primary-ion beam operated in the high current bunched mode for high mass resolution (m/Δm approximately 8000 at 29amu ($^{29}Si^+$)). A lateral resolution of 3 μm was achieved in the high current bunched mode and the pulsed ion beam target current was approximately 0.37 pA. A list of fragments of known composition (CH_3^+, $C_2H_3O^+$, $LiOH^+$, $AlOH^+$ and Al_2^+) was used to calibrate the mass spectra. The accuracy of a mass assignment (Δ in ppm) was calculated by dividing the absolute difference between the experimental (M_{ex}) and theoretical (M_r) mass of a fragment by the experimental mass, as shown below:

$$\Delta = \frac{|M_{ex} - M_r|}{M_r} .10^6 \tag{1}$$

The images of the large scribe areas after NSS exposure and the images of PB, Li-PB and Li-LDH reference samples were obtained by rastering the scribe area in patches of 400 μm × 400 μm. The analysis time of each patch was 60 s, using a pixel density of 250 pixels/mm. Based on a compositional analysis of Marcoen et al. [25], a characteristic peak list was created for the reference materials and subsequently applied to spectra obtained by large area imaging of NSS exposed scribes.

2.2.3. Compositional analysis using a multivariate analysis method (MVA)

Since every pixel of the ToF-SIMS image contains a complete mass spectrum, large area ToF-SIMS imaging provides large amounts of data. Multivariate analysis (MVA) is an efficient tool for ToF-SIMS data analysis [28]. Especially, in this work the main reason to use MVA is that the compounds of interest will share most of the secondary ions thus making them unambiguously distinguishable only via MVA methods A peak list containing, characteristic for the reference materials, was first created using the *SurfaceLab* software (IONTOF GmbH) and data cuboids containing the maps of the areas of all selected peaks were then exported as binary. BIF6 files for each large area surface analysed. The. BIF6 files were loaded into the *simsMVA* MATLAB app (http://mvatools.com) using the stitch function to perform matrix augmentation and create a single matrix containing all (stitched) patches and the reference images enabling the entire dataset to be processed as a single matrix [29]. The insertion of rows containing measurements of well-known reference materials has proven to be effective and more details of the methodology can be found elsewhere [25,28,30].

Prior to MVA, two pre-processing steps were performed: normalisation of all map intensities by total counts per pixel and Poisson scaling of the peak intensities according to a method proposed in the literature [31]. Non-negative matrix factorisation (NMF) was then applied to the resulting dataset. NMF is a non-supervised machine learning method that seeks to reduce the dimensionality of a dataset down to a few "pure compounds" [30,32]. This method enables the interpretation and visualization of the surface chemistry because it provides data that can be directly assigned to fingerprint mass-spectra of "pure" compounds and their distribution maps [30]. The algorithm used to achieve non-negative factorisation of all datasets presented in this paper is the one created by Lee and Seung [33], based on multiplicative update rules and applied by Trindade et al. [30].

3. Results and discussion

3.1. Leaching behaviour of the coatings

Leaching profiles were obtained for the Li-salt loaded coatings with 15 and 2.5% PVC Li-salt. Fig. 3 shows the accumulative inhibitor release for the coatings in mM/L during 200 h leaching. The inset of Fig. 3 shows the expanded graph for the samples with a lower Li release from the coating. From the graphs it can be noted that both Li-salt loaded coatings with 15% PVC inhibitor leach significantly faster compared to

the coatings loaded with only 2.5% PVC inhibitor. The 15% PVC Li-oxalate sample in particular leaches faster at higher concentrations of Li compared to the sample with 15% PVC Li-carbonate. These differences and of magnitude are in line with the solubility of these corrosion inhibitors being 1.3 g/100 ml for Li-carbonate [34] and 8.0 g/100 ml for Li-oxalate [35].

The inhibitor release of corrosion inhibitors from an organic coatings depends on the PVC and the quantity and solubility of the corrosion inhibitor in the coating [4]. Since all coatings in this study were formulated to a total PVC of 30%, the leaching curves demonstrate that the dissolution of Li from these coatings depends on the solubility of the Li-salt and the loading of the Li-salt in the coating.

3.2. Active protective properties from the coating

3.2.1. Optical and electron microscopy assessment of the defect area

To assess the active protective properties, the Li-loaded coatings were artificially damaged and exposed to the NSS test for 168 h. Fig. 4 shows the optical images (I) of the defect area, the top-view (II) and cross-sectional (III) scanning electron micrographs of the surface of the substrate in the defect area of the different coatings. The analysis with the optical microscope (Fig. 4(I)) showed that all coatings provide effective corrosion protection because no voluminous white corrosion products, typical for aluminium corrosion, were observed in the defect areas after the NSS exposure [20]. The highly loaded samples with 15% PVC Li-salts showed almost pristine scribes with no corrosion products. The lower loaded (2.5% PVC) samples showed some darkening but no corrosion products were observed in the defect area. The formation of the protective layer in the defect area involves a surface corrosion process whereas aluminium is anodically dissolved from the alloy matrix and forms the aluminium hydroxide layer at the aluminium surface in the defect area. The formation of such a protective layer can cause some discoloration (darkening) to the defect area. This darkening is observed in different gradations in the defect area since the optical appearance of the resulting layer in a defect area is a complex matter which is influenced by multiple factors such as scattering due to surface etching [36], the optical properties of the formed species [37], the thickness of the layer [38], and the local dissolution of other alloying elements such as magnesium which deposit at the alloy/oxide interface [39].

The SEM micrographs of Fig. 4(II) show that a protective layer was formed in the defect areas of the Li–salt loaded coatings independently of the loading level of the Li-salt in the coating. The surface morphology of the layers generated from the 15% PVC samples is similar for both the Li-carbonate and Li-oxalate samples showing a polycrystalline surface morphology representative for hydrated oxides such as layered double hydroxides [27]. The layers generated by active inhibition from the coatings with 2.5% PVC Li-salts have a slightly different surface morphology compared to the 15% PVC samples. Whereas the Li-carbonate sample (Fig. 4a(2.5% (II))) featured a finer structure compared to the 15% loaded sample, the Li-oxalate sample showed a more porous surface morphology (Fig. 4b(2.5% (II))). However the cross-sectional analysis (Fig. 4(III)) revealed that the thickness of the generated protective layers was approximately 1.0–1.5 μm for all samples and featured a similar morphology typical for Li-leaching coatings with a dense inner layer and a porous outer layer [20].

3.3. Corrosion inhibition of large defect areas

3.3.1. Optical analysis of large defect areas after NSS

The corrosion inhibiting reach (throwing power) of these coatings was assessed by exposing panels with increasing scribe widths from 0.5 mm up to 6 mm (Fig. 5) with a vertical orientation in the NSS for 168 h. Fig. 5 shows the partial scribe areas after the NSS exposure. Fig. 5a shows the detrimental corrosion effects in the defect areas on AA2024-T3 when a coating has no corrosion inhibitor, All scribes are
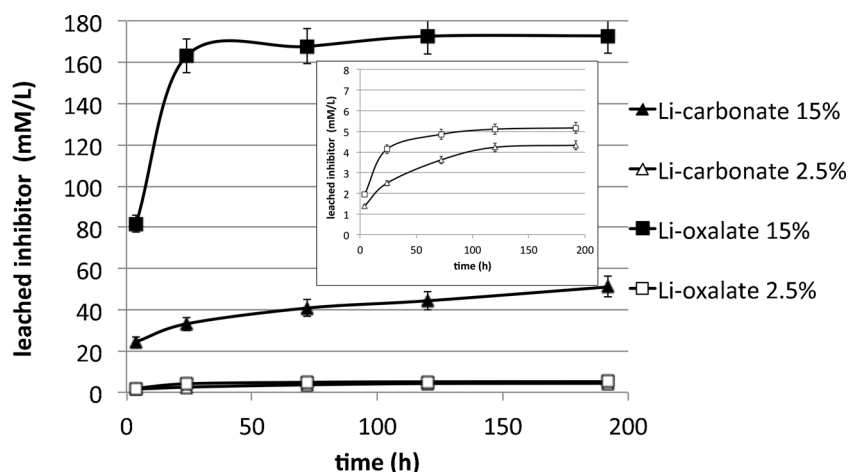
Fig. 3. Accumulated release of corrosion inhibitor from coatings containing high (15% PVC) and low (2.5% PVC) loadings of Li-salt, normalized per cm² model coating with a thickness of 25 µm over a 192 h exposure time period.
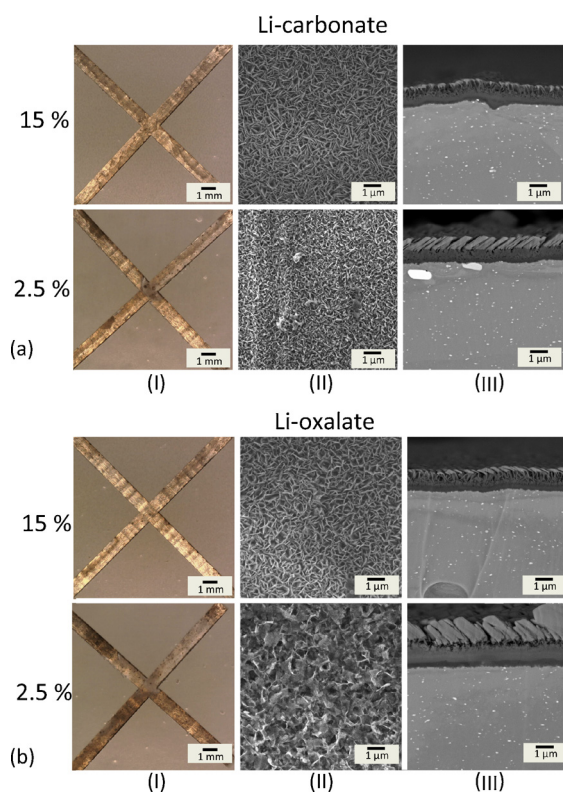

Fig. 4. Optical and scanning electron microscopy analysis of the defect areas of Li-leaching coatings after 168 h NSS exposure: (a) Li-carbonate loaded coating (15 and 2.5% PVC) and (b) Li-oxalate loaded coating (15 and 2.5% PVC). (I) optical microscope image of the defect area; scanning electron micrograph of (II) the defect area in planar view; (III) cross-sectional view of the defect area.

severely affected by corrosion in this case. In addition to several pits, large amounts of voluminous white corrosion products can be observed. The images in Fig. 5b show the effect of the coatings loaded with 15% and 2.5% PVC-carbonate. Both coatings with high and low loading show effective corrosion inhibition in the defect areas up to 3 mm. The 6 mm scribe is even protected by the 15% PVC Li-carbonate sample, whereas the sample with 2.5% PVC Li-carbonate shows some darkening and some white corrosion products on the left hand side of the defect which indicates that locally the active corrosion protection was not sufficient. A similar behaviour is observed for the Li-oxalate based coatings in Fig. 5c. Both coatings loaded with 15% and 2.5% PVC Li-

oxalate show almost well protected scribes without signs of corrosion products in the scribes up to 3 mm wide. Like the Li-carbonate loaded samples, the difference in throwing power can be observed in the scribe with a width of 6 mm. Whereas the 15% PVC Li-oxalate loaded coating shows complete passivation of the area without the presence of white corrosion products, the 6 mm scribe of the 2.5% PVC Li-oxalate shows several pits and some white corrosion products. These results show that it is possible to protect large defect areas (up to 6 mm) with the Li-leaching technology. Local and superficial dealloying has been observed as part of the formation of the protective layer in the defect area after 168 h NSS exposure. This phenomenon of limited local attack can be observed by the presence of several small black pits in the defect area which have not lead to significant active pitting corrosion as observed in Fig. 5a. Hence, from the results in Fig. 5 it can be concluded that Li-leaching coatings are able to protect large defect areas. Even the coating with only 2.5% lithium salts and slow litium release kinetics are able to provide effective corrosion inhibition. These observations underline the active protective nature of Li-leaching coatings.

3.3.2. Surface roughness in the defect area

White light interferometer (WLI) profilometry was used to measure the surface roughness (Sa) in the defect areas to obtain absolute values for the degree of corrosion in the defect areas as a result of local corrosion phenomena such as pitting corrosion [40]. Fig. 6a shows a graph with the surface roughness values of the different scribes before and after 168 h exposure to NSS. This graph shows the effect of the active protective nature of the Li-salts when used as leachable corrosion inhibitors. The graph confirms the damaging effect in the defect area when the coating does not provide active corrosion protection. The Sa increases with increasing scribe width from 0.5 µm before exposure to values of 2.5 to 3.5 µm in scribes of 3 mm and 6 mm due to the effects of general and local corrosion processes in the defect area after exposure. The surface roughness of the Li-leaching coatings increases only slightly compared to the unexposed samples. Fig. 6b shows the WLI surface roughness maps of the 3 mm scribes highly loaded coatings before and after 168 h NSS exposure. The uninhibited sample shows large areas that were affected by (pitting) corrosion. The 3 mm scribes of the 15% PVC Li-leaching coatings have a smooth surface with only a few very small pits. These results confirm the efficient active protective properties of Li-salts when used as leachable corrosion inhibitors in organic coatings.

3.3.3. Scanning electron microscopy analysis of wide scribes

Fig. 7 displays the SEM micrographs of the widest scribes of the Li-leaching coatings with the best inhibition performance focussing on (I)
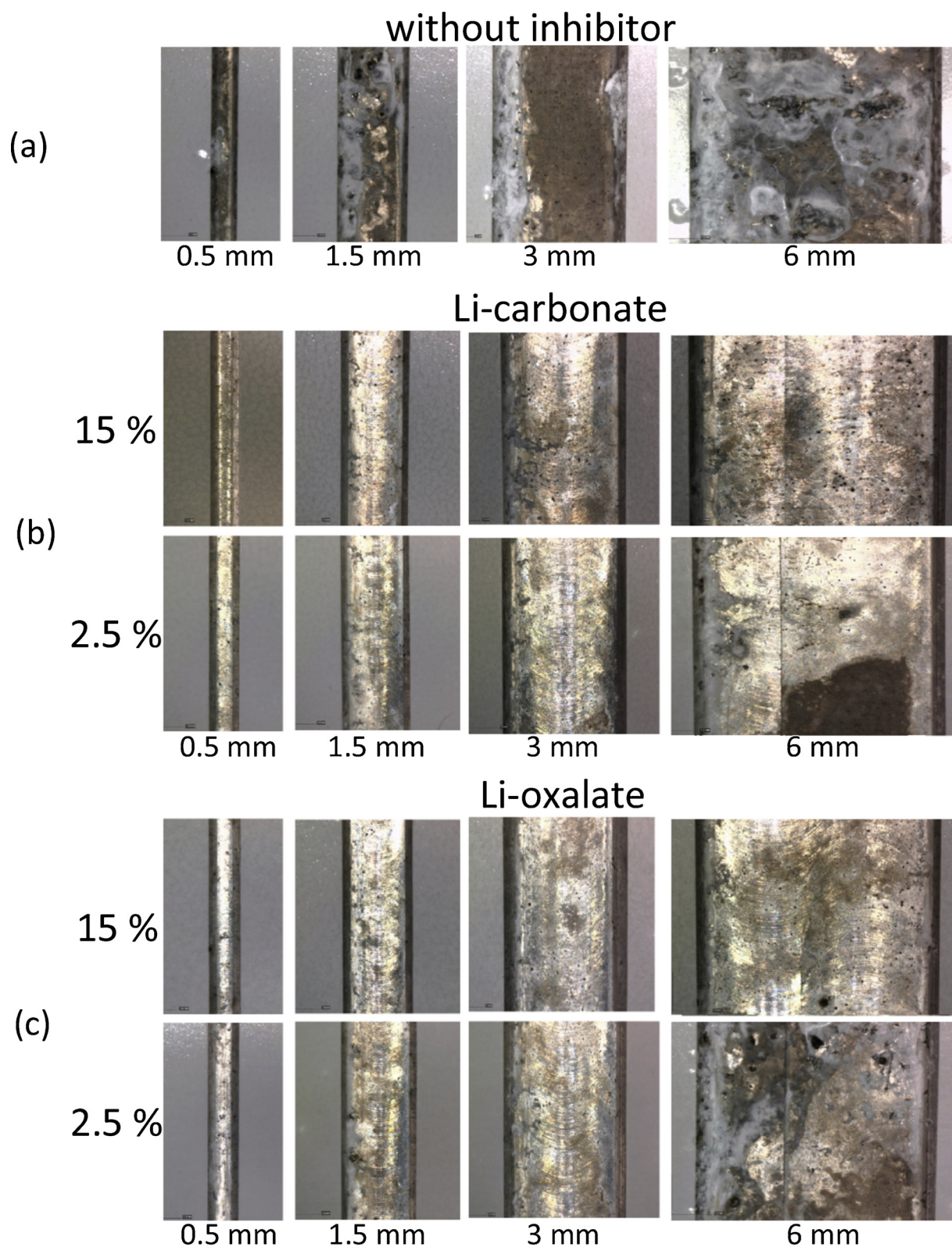
without inhibitor

(a)

0.5 mm   1.5 mm   3 mm   6 mm

Li-carbonate

15 %

(b)

2.5 %

0.5 mm   1.5 mm   3 mm   6 mm

Li-oxalate

15 %

(c)

2.5 %

0.5 mm   1.5 mm   3 mm   6 mm

Fig. 5. Optical images of the defect areas with different scribe widths (0.5 mm, 1.5 mm, 3.0 mm and 6.0 mm) after 168 h NSS exposure of coatings loaded with (a) no active corrosion inhibitor; (b) Li-carbonate (15 and 2.5% PVC); (c) Li-oxalate (15 and 2.5% PVC).

the top view appearance of the scribe, (II) the morphology of the protective layer, and (III) the cross-sectional analysis. The 6 mm scribe was investigated for the samples with 15% PVC Li-salt (Fig. 7a and c) and the 3 mm scribe was selected for the samples with 2.5% PVC Li-salt (Fig. 7b and d). The top view analysis in Fig. 7(I) of the scribes showed

no signs of pitting corrosion for all the samples investigated. The fast effective inhibition of the Li-leaching coatings preserved the machining patterns resulting from the scribing process. At higher magnification the protective layer was revealed (Fig. 7(II)) showing a very different surface morphology for all samples compared to observations in the
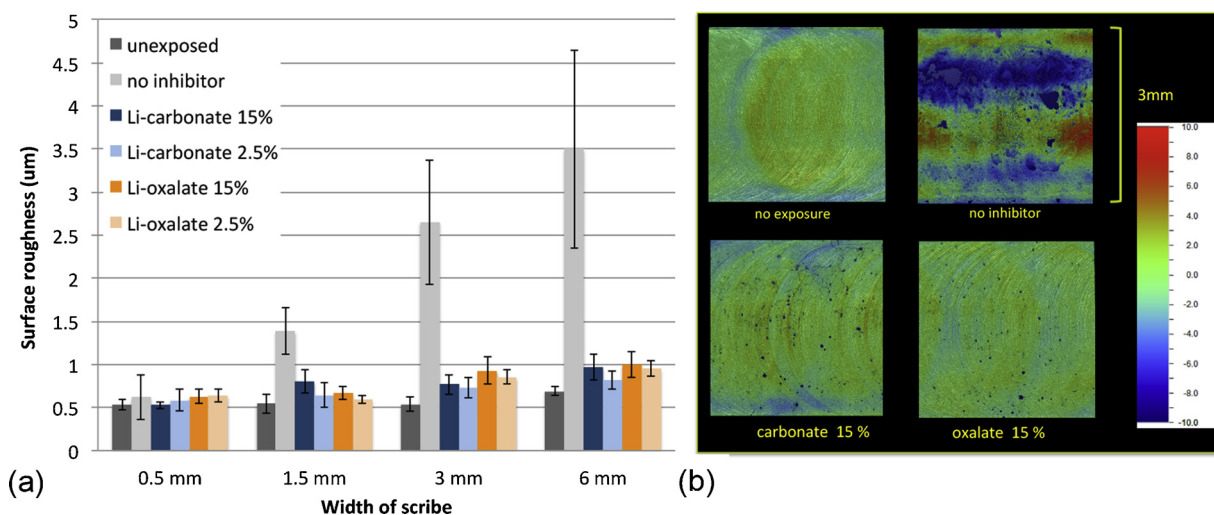
Fig. 6. Surface roughness (Sa) of (a) the defect areas displayed in Fig. 5 acquired by WLI measurements; (b) typical WLI surface maps of the 3 mm wide scribes prior to exposure as well as for coatings without inhibitor and coatings with a high loading of Li-carbonate and Li-oxalate.

1 mm scribes as shown in Fig. 4. None of the samples shows the characteristic polycrystalline morphology. The cross-sectional analysis (Fig. 7(III)) revealed that all scribes were covered with a protective layer. The Li-carbonate samples showed a thin protective layer of 240–280 nm in the 6 mm scribe of the 15% PVC sample (Fig. 7a(III)) and a layer with an approximate thickness of 1.0 µm in the 3 mm scribe of the 2.5% PVC Li-carbonate sample (Fig. 7b(III)). The Li-oxalate loaded samples showed slightly thicker layers of 1.0 µm and 1.2 µm for the 15% PVC and 2.5% PVC samples respectively (Fig. 7c and d(III)).

3.4. Li-spread and compositional analysis using time-of-flight secondary ion mass spectrometry

Li is a difficult element to detect with regular surface analytical techniques, due to its low atomic number. In this work, the surface composition of the protective layer formed in a defect on AA2024-T3 from Li-leaching was studied using time-of-flight secondary ion mass spectrometry (ToF-SIMS). It was aimed to analyse the layer's surface composition(s) and the distribution of lithium in the defect area. ToF-SIMS has a large sensitivity towards lithium and it has demonstrated its ability to identify the chemical speciation of inorganic compounds [41]. ToF-SIMS provides compositional data of the very surface of the protective layers, but in combination with the high lateral resolution of the technique, the lateral spread of the lithium based species within defect areas after NSS exposure could be imaged. Characteristic ion-fragment assignments were made and a multivariate analysis method non-negative matrix factorisation (NMF)) was applied to identify the various species present at the surface of the protective layer.

3.4.1. Non-negative matrix factorization (NMF) method

Previous ToF-SIMS work made it possible to observe the lateral Li-distribution in the defect area and to identify and determine relative concentrations of two chemical compositions (Li-PB and Li-LDH) present at the surface of the protective layer in 1 mm defect areas [25]. In this work, the NMF methodology was extended to identify and map the distribution of three chemical compositions at the surface of the protective layers generated in the defect area: PB, Li-PB and Li-LDH. Fig. 8a–g shows the different steps involved in this procedure (Fig. 8a). An optical image of the defect area to be analysed is shown (Fig. 8b). Large area ToF-SIMS images (total ion maps are shown) are obtained for the defect area and for three reference materials (PB, Li-PB and Li-LDH). Each pixel contains a full mass spectrum (Fig. 8c). Nineteen fragments of interest, characteristic for the reference materials were selected based on a compositional ToF-SIMS analysis [25]. Each

fragment has its own map, as shown for $^6Li^+$, Li_2OH^+ and $AlO_2H_2^+$ [25] (Fig. 8d). All data cubes from the maps of defect area for the three compounds of interest and three reference compounds were stitched into a single data set. Given that three different reference materials were included in the dataset, the entire dataset was processed with NMF into three pure compounds according to the method of Trindade et al. [30] (Fig. 8e). The resulting NMF output provides, on one hand the fingerprint spectra of the three reference materials and on the other hand, the normalized NMF intensities of the pure compound were plotted per pixel in an overlay map in the defect (Fig. 8f). In order to determine the percentage of surface coverage for each compound, each pixel was assigned to a single compound, based on thresholds applied to the NMF intensities. Each compound is mapped separately for the defect area (Fig. 8g). Based on the total amount of pixels, these normalized NMF intensities can be converted into a compositional ratio of the pure compounds present at the surface of the protective layer in the defect area.

3.4.2. Lithium spread and composition in a defect area over time

ToF-SIMS analysis of the surface composition in the defect area, as described above was applied on samples of the 15% PVC Li-carbonate loaded coating to study the Li-spread and the surface composition of the protective layer in the 1 mm wide scribe as a function of NSS exposure time (Fig. 9). The minor isotope $^6Li^+$ was used to visualise the distribution of Li ions within the defect area, as the high ionisation cross section of Li means that the $^7Li^+$ fragment was too intense and saturated the detector (Relative abundances: $^7Li^+$ = 92.5% and $^6Li^+$ = 7.5%) [25]. Fig. 9a shows the $^6Li^+$ maps as function of the NSS exposure time. These maps reveal the fast Li-spread in the defect due to the leaching of the Li-carbonate from the coating. From the surface maps it can be noted that the defect area is already completely covered with Li-compounds after only after 15 min of NSS exposure. Furthermore, the images show the Li-spread initiating at the edges of the defect area and interacting with specific areas in the defect area. The different Li concentrations observed in the $^6Li^+$ map can indicate the presence of different surface compositions in the defect area. It can be noted that over longer exposure time Li spreads out further. After 2 h NSS exposure the entire scribe was covered with a homogeneous concentration of Li. Further Li-enrichment is visible after 48 h exposure. The NMF procedure was used to reveal evolution of the surface composition of the generated layer in the defect areas after different NSS exposure times. The complete data set was factorised by NMF using the data of the three reference samples. Fig. 9b shows the NMF overlay maps of the respective ToF-SIMS $^6Li^+$ maps of Fig. 9a, representing the normalized
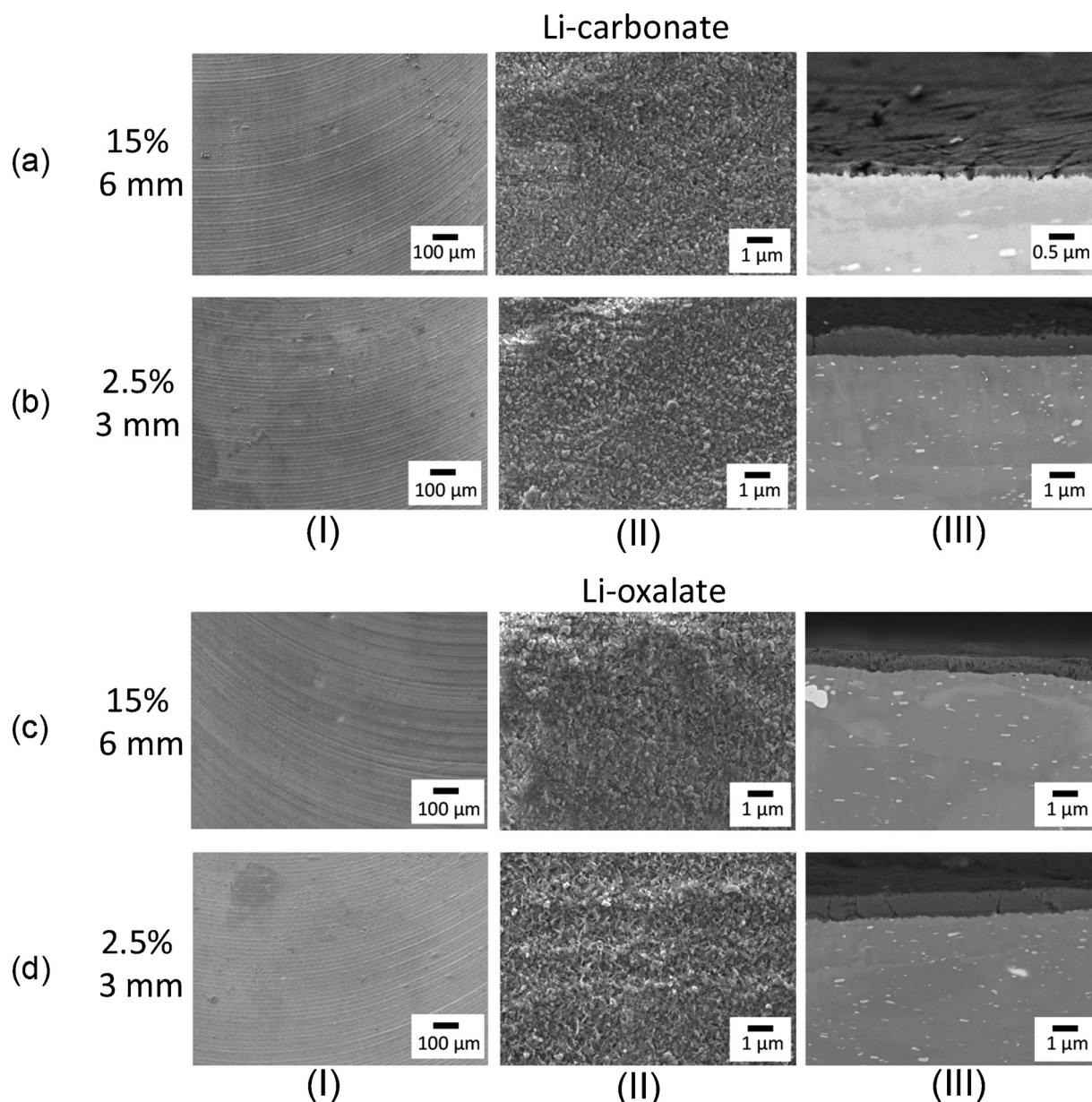
Fig. 7. Scanning electron micrographs of the defect areas of the Li-leaching coatings after 168 h NSS exposure: Li-carbonate loaded coating (a) 15% PVC, 6 mm wide defect area; (b) 2.5% PVC, 3 mm wide defect area; Li-oxalate loaded coating (c) 15% PVC, 6 mm wide defect area; (d) 2.5% PVC, 3 mm wide defect area. (I) planar view of the defect area; (II) top view of the protective layer; (III) cross-sectional view of the protective layer in the defect area.

NMF intensities of PB, Li-PB, and Li-LDH as a function of exposure time. These maps show the fast lateral spread of the Li-based compounds in the defect. After only 15 min NSS exposure, the entire defect area was basically covered with two Li based compounds, Li-PB and Li-LDH. The Li-PB layer was generated almost instantly throughout the coating defect whereas Li-LDH was formed along the edges of the defect area. Initially, Li-LDH was generated only at selective areas in the defect area (1–2 h) but longer NSS exposure resulted in the lateral spread of Li-LDH throughout the entire defect area. Fig. 9c shows the NMF intensities of PB, Li-PB, and Li-LDH detected in the defect area as a function of NSS exposure time. After only 15 min NSS, 37% of the relative surface coverage could be attributed to Li-LDH. This value increased to 94% Li-LDH surface coverage after 48 h NSS exposure.

These results revealed the very fast action of Li-salts in the coating defect when released from the coating matrix and show that two main compounds are involved in the formation of the protective layer in the defect area. Initially, the leaching of Li-ions into the defect area results

in a Li-PB layer throughout the defect area. Further leaching of Li-carbonate in the defect area due to extended exposure to the NSS conditions provide conditions that contribute to the formation of a Li-LDH throughout the defect area. Under these conditions, only small amounts, if indeed any, PB were detected.

3.4.3. Li-spread and compositional analysis in large coating defects

The previous section demonstrated that the 15% PVC Li-carbonate loaded coating was able to cover the entire 1 mm defect area fast and effectively with a Li-LDH layer demonstrating a sufficient degree of chemical throwing power for the 15% PVC Li-carbonate sample under these conditions. The same ToF-SIMS methodology was applied on the coated panels with increasing scribe widths, which were optically assessed earlier in this work to determine the lateral chemical throwing power of the coatings with high and low Li-salt loadings after 7d NSS exposure. Fig. 10 shows the Li^+ distribution maps (top rows) of a section of the scribes including the normalized total Li^+ counts per
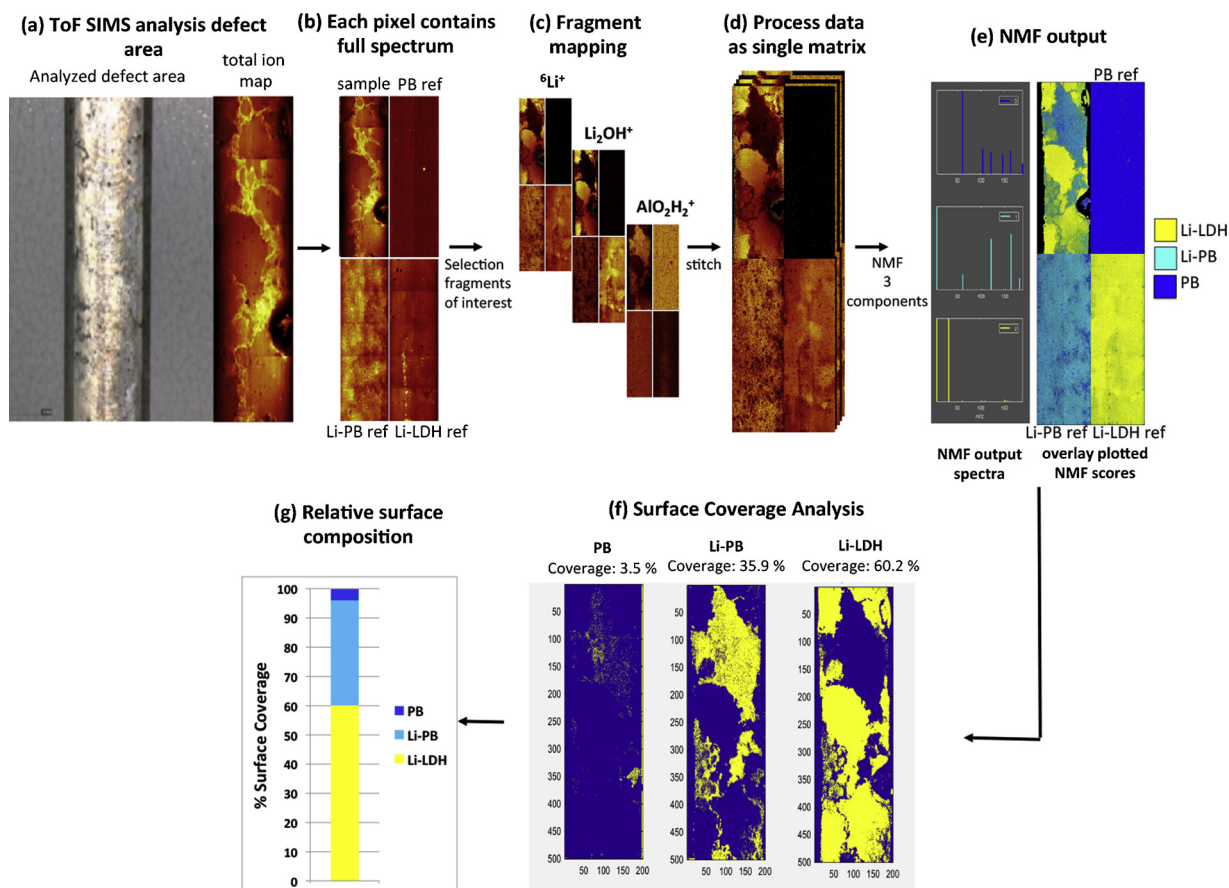
Fig. 8. Schematic description of the NMF process used for the compositional study of the corrosion protective layer in the defect area formed by the Li-leaching coatings.

mm^2 and the corresponding NMF image overlays (bottom rows). The ToF-SIMS analysis was performed in each defect area with the exclusion of the areas close to the sides of the scribe to avoid artefacts due to edge effects of the scribe. The Li^+ distribution maps show that Li is detected throughout all scribes, even up to 6 mm scribe widths after the 7 d NSS exposure. This demonstrates that all coatings with a fast leach rate

(15% PVC Li-salts) and a relatively low leach rate (2.5% PVC Li-salts) were able to generate conditions in the defect areas that enabled the formation of a protective layer on the aluminium alloy. The highest concentrations of Li^+ (counts/mm^2) were detected in scribes of the coatings with the 15% PVC Li-salt loaded coatings (Fig. 10a and c). and Li^+ concentrations decreased with increasing scribe widths. Higher
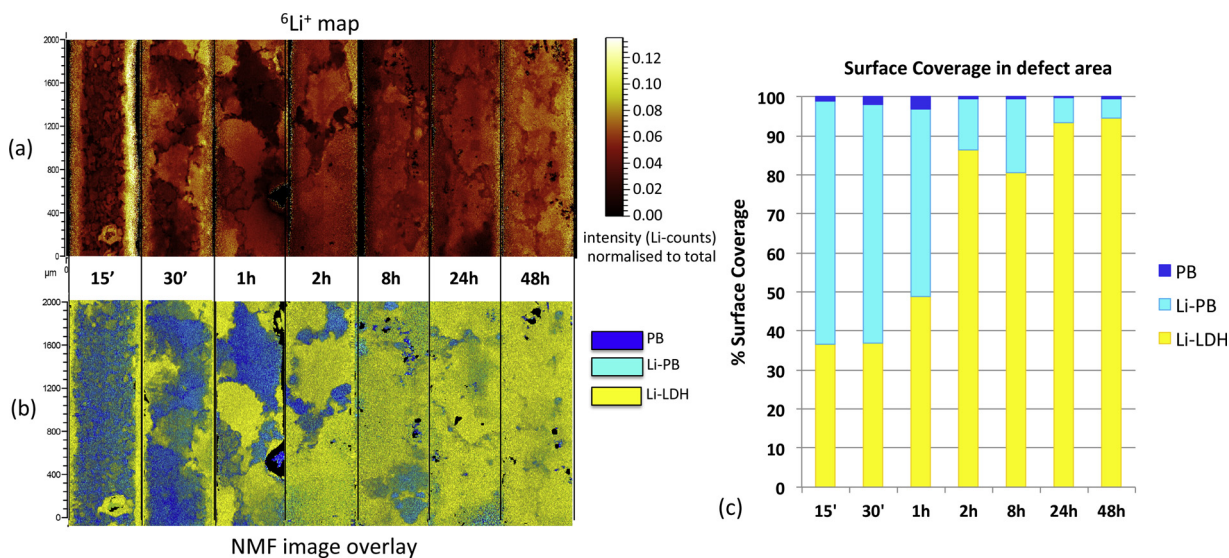

Fig. 9. Li-spread and compositional analysis during the formation of a corrosion protective layer in a 1 mm wide defect area from a 15% PVC Li-carbonate loaded coating as a function NSS exposure time: (a) $^6Li^+$ maps; (b) Overlay images of normalised NMF intensities; (c) Relative surface composition of the corrosion protective layer in the defect area for PB, Li-PB and Li-LDH after 15 min up to 48 h NSS exposure.
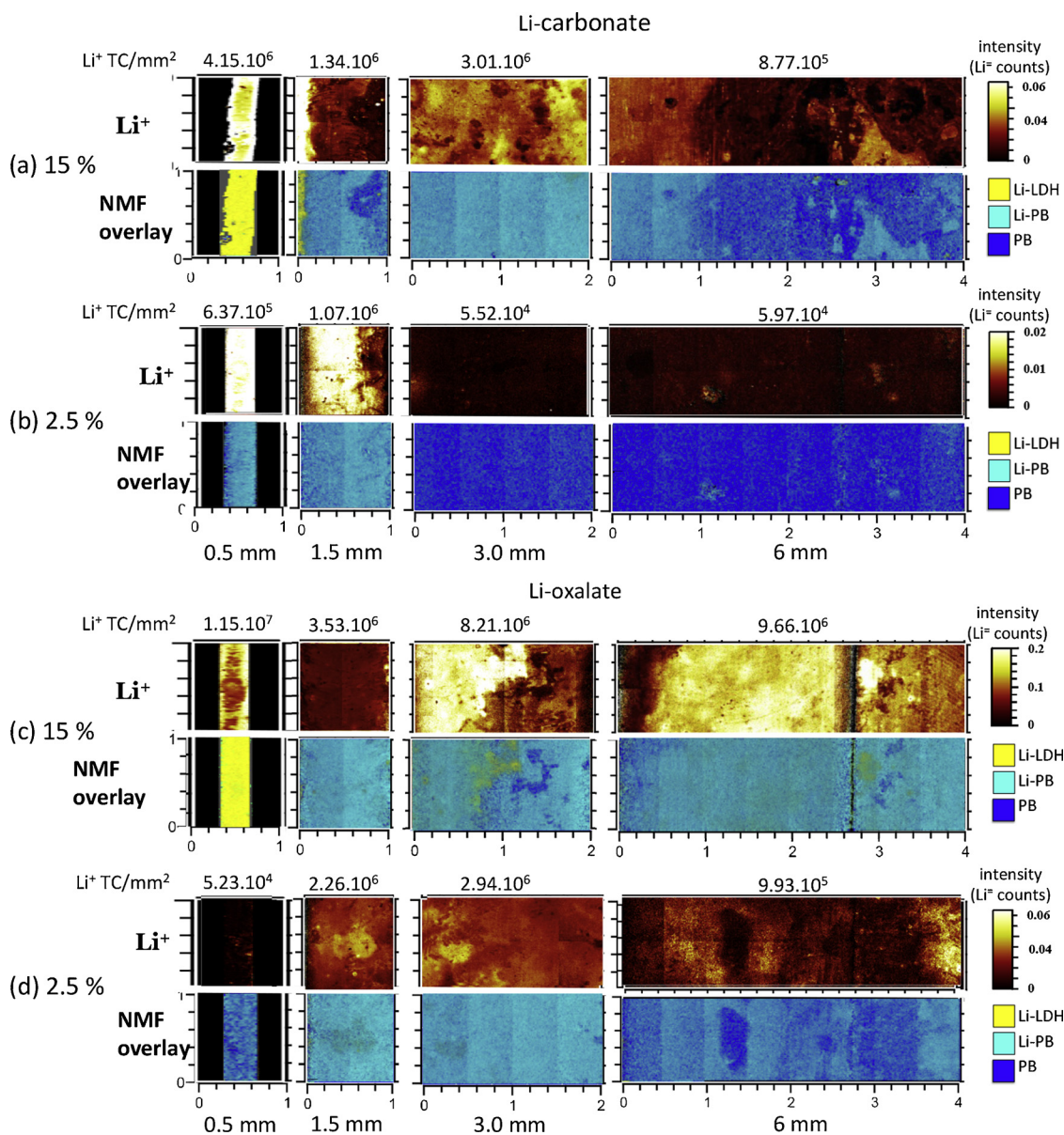
Fig. 10. Lithium spread (top row) and normalized Li$^+$ counts with the corresponding NMF image overlay images (bottom row) of the corrosion protective layers generated in the defect areas (0.5 mm, 1,5 mm, 3.0 mm and 6.0 mm width) from the Li-carbonate loaded coating (a) 15% PVC; (b) 2.5% and the Li-oxalate loaded coating (c)15% PVC; (d) 2.5% PVC.

concentrations of Li$^+$ were detected in the scribes of the Li-oxalate loaded coatings compared to the Li-carbonate coatings. This is in line with the faster leach rate of the Li-oxalate loaded coatings. The concentrations of Li$^+$ distributed in the defect areas of the 2.5% PVC loaded samples were clearly lower than the 15% PVC loaded samples. However, the defect areas up to 6 mm were still covered with Li-containing compounds. This demonstrates the mobility, reactivity and the chemical throwing power of the lithium-ions, even at low concentrations.

The NMF procedure was applied on these samples to generate compositional maps of the surface chemistry and to distinguish a relative quantification of pure compounds in the defect areas using three reference samples (PB, Li-PB, and Li-LDH). The bottom rows of each figure in Fig. 10 show the NMF overlay images showing the distribution of the three compounds in the analysed defect areas. The NMF overlay images of Fig. 10a show that the surface of the 0.5 mm defect of the 15% PVC Li-carbonate is fully covered with Li-LDH. However, it can be observed that the surface composition of the wider defect areas can be

attributed to Li-PB and that Li-LDH is not detected. Fig. 10b shows the uniform distribution of Li$^+$ in the defect areas of the 2.5% PVC Li-carbonate coatings. The NMF overlay maps of these defect areas reveal that little or no Li-LDH was formed in these defect areas but these defect areas where covered with a protective layer composed of a mixture of Li-PB and PB. A similar behaviour was observed for the Li-oxalate coatings in Fig. 10c and d. The NMF analysis showed that the relative surface composition of the protective layer in the 0.5 mm defect of 15% PVC Li-oxalate coating (Fig. 10c) comprises mainly Li-LDH, whereas the surface composition of protective layers in the wider scribes contain primarily Li-PB with some local areas of Li-LDH. The protective layers in all defect areas of the 2.5% PVC Li-oxalate coated samples comprise mainly Li-PB.

Fig. 11 summarizes the relative surface composition intensities of the 3 pure compounds detected at the surface of the protective layer in the defect derived from the NMF procedure applied on the samples with increasing defect widths. For the 15% PVC Li-carbonate loaded coating (Fig. 11a) it can be observed that the occurrence of Li-LDH decreases
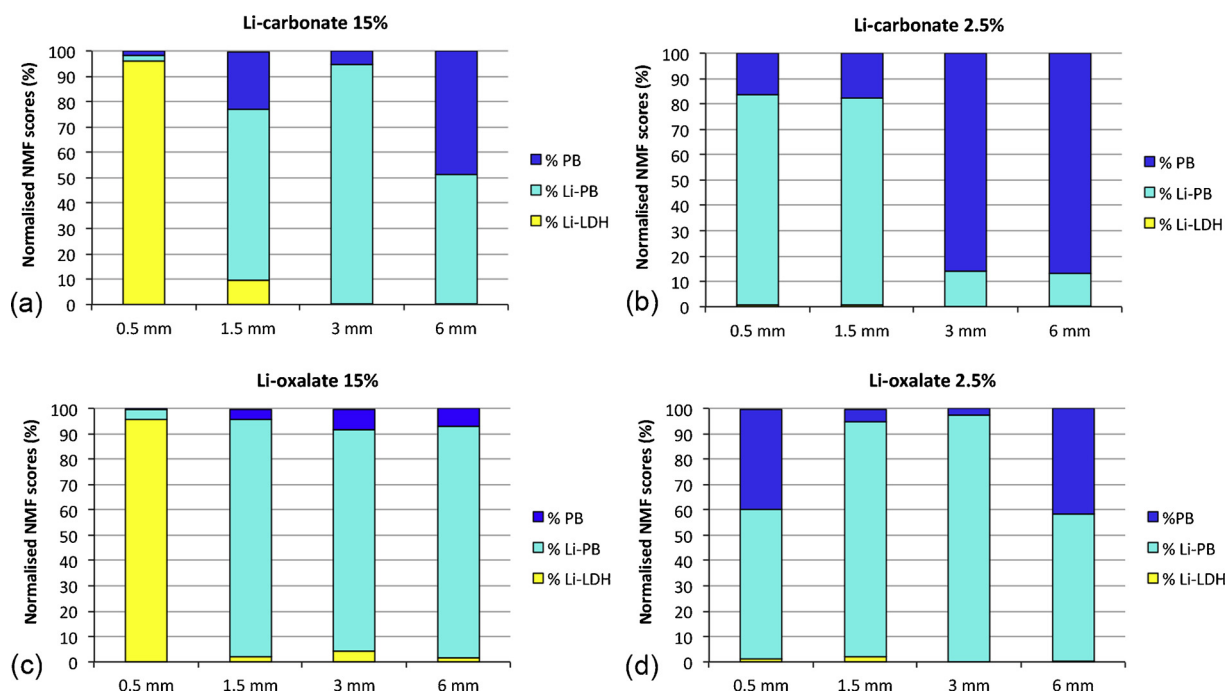
Fig. 11. Relative surface composition of the corrosion protective layer in the defect areas (Li-LDH vs. Li-PB) obtained from the NMF image overlay data displayed in Fig. 10: Li-carbonate loaded coating (a) 15% PVC; (b) 2.5% PVC and Li-oxalate loaded coating (c) 15% PVC and (d) 2.5% PVC.

rapidly when the defects become wider. The coverage with Li-LDH drops from 95% in a 0.5–1 mm scribe to values below 10% when the defects becomes 1.5 mm or wider. Instead of Li-LDH, Li-PB becomes the most abundant species. A similar trend is observed for the 15% PVC Li-oxalate samples in Fig. 11c. Li-PB is also the most abundant species found at the surface of the protective layer throughout the defect areas of the 2.5% PVC Li-salt coatings (Fig. 11b and d). Only in the wider scribes of the 2.5% PVC Li-carbonate the levels of Li are lower at the surface of the protective layer and the majority of the species in the defect area can be related to PB.

In summary, the graphs of Figs. 10 and 11 imply that the surface composition of the protective layer in the defect areas depends on the inhibitor release rate and loading of the coating and the size of the defect. The occurrence of Li-LDH seems to be related to systems with fast leaching and high Li-loading (15% PVC Li-salts) and relatively small defect widths (0.5 mm). These parameters will result in high Li concentrations and alkaline conditions which are favourable for the formation Li-LDH [27].

A surprising and novel observation from this work is that the main surface compound of protective layers generated in the wider scribes and slower leaching systems can be identified as Li-PB. For the 2.5% PVC Li-carbonate coatings the contribution of PB in surface layer increases with scribe width. The combination of these observations with the knowledge that the defect areas were effectively protected, leads to the conclusion that Li-LDH is not the key corrosion inhibiting species needed for effective corrosion inhibition but in essence appears to be a side-product which is generated when high levels of Li carbonate and oxalate are present in the defect area.

3.5. Chemical throwing power of Li-leaching coatings

The approach in this study confirmed the important aspects that are considered as essential for effective active corrosion protection from organic coatings. In order to have a sufficient chemical throwing power, coatings must be able to leach sufficient amounts of corrosion inhibitor to achieve a critical inhibitor concentration in the defect area in a short time to obtain a fast and irreversible corrosion inhibition [12,15]. However, it is known that the larger the defect size is, the more difficult

it is to obtain these critical concentrations of corrosion inhibitor in the defect to prevent corrosion [14].

In the work discussed above, Li-leaching coatings were investigated varying inhibitor loading, inhibitor solubility and defect size to obtain more insight in the throwing power characteristics of this novel chromate-free active protective coating technology. These factors contribute to the inhibitor accumulation in the defect area and the efficacy of the Li-based coating technology. The results of the investigation showed that the investigated Li-leaching coatings have a chemical throwing power of 3 to 6 mm and the ability to cover and protect these wide defect areas effectively. The ToF-SIMS analysis of the defects areas revealed that Li is distributed throughout the defect areas and three different compounds (Li-LDH, Li-PB, and PB) were found. The ratio of these compounds seems to be related to the dissolution of the corrosion inhibitor from the coating matrix (i.e. loading in the coating and solubility of the Li-salts). The work indicates that Li-LDH is a side-product in the generation of these protective layers due to fast release of the Li-salts leading to high Li concentrations and high pH values in small defect areas.

With these results, it is possible to discuss the proposed formation mechanism of these protective layers from lithium leaching coatings in more detail (Fig. 12) [21,39]. Considering the possible event of a coating defect, the aluminium alloy AA2024-T3 will be exposed to environmental conditions and a thin layer of electrolyte will be formed in the defect. This moisture will trigger the dissolution and diffusion of the Li-salt from the organic coating matrix into the defect area initiating Stage I of the formation mechanism. Due to the alkalinity of the Li-salts, the conditions in the defect area will become alkaline (pH 9–10) and the presence of chlorides in the electrolyte the natural oxide of the aluminium alloy will be thinned [21,42]. This oxide thinning will enable the initial formation of the protective layer (Stage II) via direct anodic dissolution of aluminium, resulting in the formation of aluminium hydroxide gel on the aluminium substrate under these moderate alkaline conditions [43,44]. When the film of aluminium hydroxide gel covers the surface, the layer will develop by a growth and dissolution process until a stable state is reached. This growth and dissolution process (Stage III) is characteristic for aluminium in alkaline conditions [20,27,45–47]. Stages I and II are known to be fast processes and the
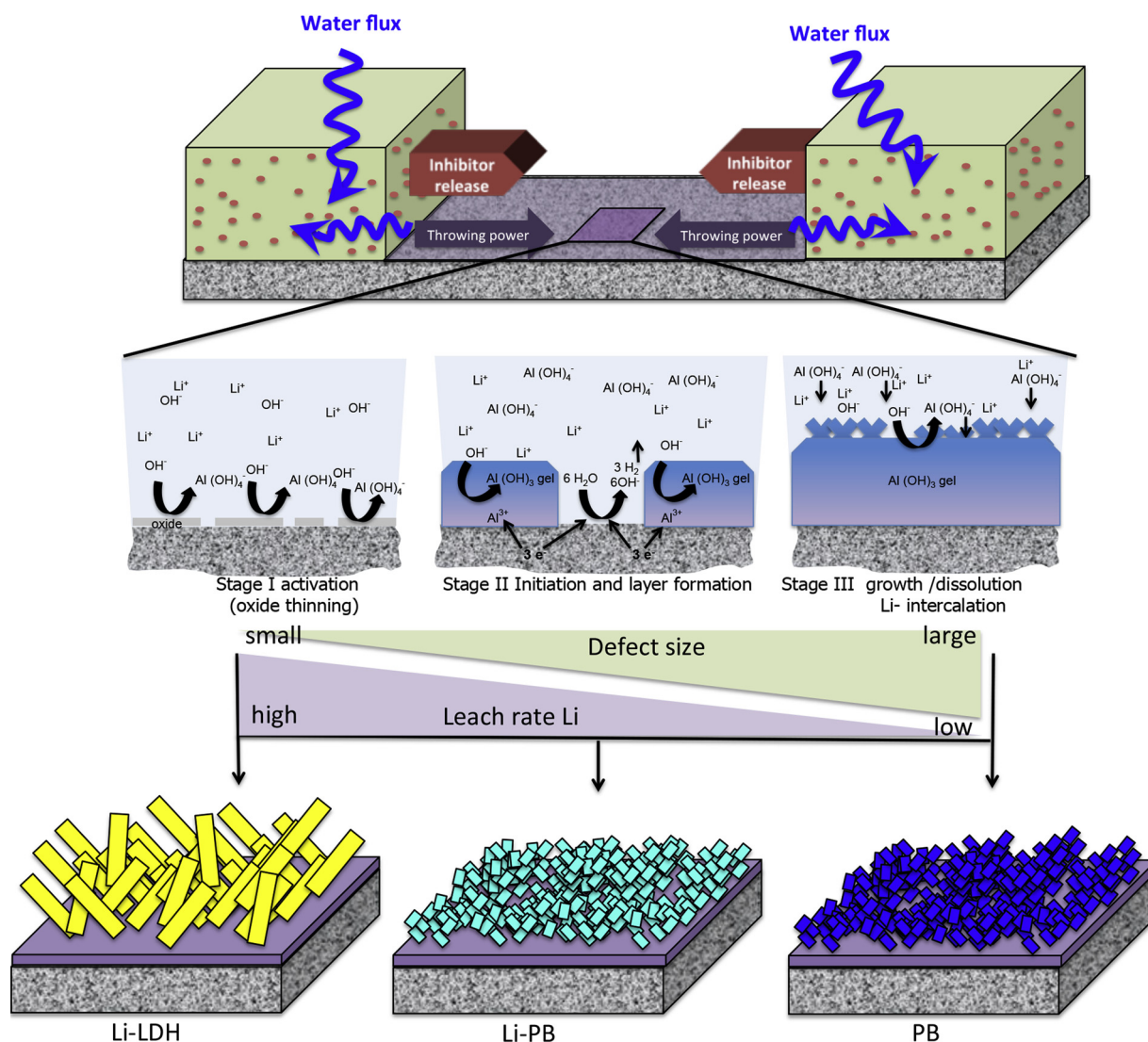
Fig. 12. Schematic illustration of the mechanism and the relation between the surface composition of the protective layer in the defect related to the Li leach rate and the size of the coating defect.

growth-rate in stage III is limited by diffusion of species across the dense inner oxide [44,48]. This oxide growth process may be accelerated by the presence of chloride ions which are thought to be able to facilitate the hydration and dissolution process of amorphous oxide.

This aluminium corrosion process results in a surface-covering layer on the aluminium alloy with a dense morphology at the inner layer near the aluminium alloy/(hydr)oxide interface and a porous morphology at the outer region of the protective layer. From the results obtained in this work, it became apparent that three different compounds can be identified at the outer region of the protective layer: (i) Li-LDH: in the case of high Li concentrations and small defect areas; (ii) Li-PB: in the case of moderate Li concentrations and wider defect areas and (iii) PB: in the case low Li concentrations and wide defect areas.

It is known that Li-LDH can be formed when there is sufficient Al $(OH)_4^-$, Li^+, CO_3^- or OH^- in solution at pH values higher than 10 [27]. On the other hand, it is known that amorphous aluminium hydroxide transforms into pseudo-boehmite by an aging process in mildly alkaline conditions [44]. The results from this research indicate that Li-LDH is not the primary corrosion inhibiting species in the defect area from these Li-leaching coatings and that the relative Li^+ concentration in the defect area determines whether Li-LDH is formed or not.

Li-PB was the most prominent surface species detected in most of the defect areas. It is known that ions (e.g Cerium) [26] can be

incorporated in pseudoboehmite layers promoting oxide growth [26]. The results show that most of the defect areas are protected by PB layers with high and low amounts of Li depending on the leach rate and width of the defect area. This combined with the Li distribution in the defect areas strongly suggests that Li is involved in the stabilization of the aluminium hydroxide layer in the defect area. However, additional studies are needed to explain the chemical stabilization mechanism of the aluminium hydroxide layer by Li. In addition this work, demonstrated the chemical throwing power properties of lithium-leaching coatings and has shown that only small amounts or low concentrations of Li are needed to provide active corrosion protection in large defect areas. The efficacy of the corrosion protection seems to be limited by the amount of Li that can be released from the coating into the defect area and the ability to reach the critical concentration and conditions for effective corrosion inhibition. The insights obtained in this work provide an enhanced view on the active corrosion inhibiting properties and the mechanism of Li-leaching coatings for the protection of aluminium alloys

4. Conclusions

This work studied the chemical throwing power of Li-leaching coatings and the compositional analysis of the protective layers in the

coating defects. Organic coatings were formulated with different Li-salts as corrosion inhibitors and different loadings to obtain different leaching behaviours to evaluate the distance (throwing power) these leaching Li-inhibitors are able to protect coating defects with increasing widths.

It was demonstrated that Li-inhibitors were able to protect coating defects with a width up to 6 mm from coatings with different leaching behaviours by the formation of a protective layer in the defect area.

ToF-SIMS was used to map the distribution and relative concentration of lithium in the defect areas. An NMF analysis of the ToF-SIMS datasets was applied to link the Li distribution in the defect areas with the compositional characterisation of the surface of the protective layer. It was found that Li-PB is the main surface compound encountered and Li-LDH is a side-product, which is generated in small defect areas and at fast Li-leaching rates.

This study provides a further understanding of the active corrosion protective properties, the surface composition in the defect and demonstrates the chemical throwing power of the Li-leaching technology, a feature that has not been demonstrated for any other chromate-free inhibitor leaching coating technology.

Acknowledgements

References

[1] I.M. Zin, R.L. Howard, S.J. Badger, J.D. Scantlebury, S.B. Lyon, The mode of action of chromate inhibitor in epoxy primer on galvanized steel, Prog. Org. Coat. 33 (1998) 203–210.

[2] M.A. Jakab, J.R. Scully, On-demand release of corrosion-inhibiting ions from amorphous Al–Co–Ce alloys, Nat. Mater. 4 (2005) 667.

[3] P. Klomjit, R.G. Buchheit, Characterization of inhibitor storage and release from commercial primer, Prog. Org. Coat. 114 (2018) 68–77.

[4] S.G.R. Emad, X. Zhou, S.B. Lyon, G.E. Thompson, Y. Liu, G. Smyth, D. Graham, D. Francis, S.R. Gibbon, Influence of volume concentration of active inhibitor on microstructure and leaching behaviour of a model primer, Prog. Org. Coat. 102 (2017) 71–81.

[5] F.H. Scholes, S.A. Furman, A.E. Hughes, T. Nikpour, N. Wright, P.R. Curtis, C.M. Macrae, S. Intem, A.J. Hill, Chromate leaching from inhibited primers. Part I. Characterisation of leaching, Prog. Org. Coat. 56 (2006) 23–32.

[6] S.A. Furman, F.H. Scholes, A.E. Hughes, D. Lau, Chromate leaching from inhibited primers. Part II: modelling of leaching, Prog. Org. Coat. 56 (2006) 33–38.

[7] T. Prosek, D. Thierry, A model for the release of chromate from organic coatings, Prog. Org. Coat. 49 (2004) 209–217.

[8] A.E. Hughes, A. Trinchi, F.F. Chen, Y.S. Yang, I.S. Cole, S. Sellaiyan, J. Carr, P.D. Lee, G.E. Thompson, T.Q. Xiao, The application of multiscale quasi 4D CT to the study of SrCrO4 distributions and the development of porous networks in epoxy-based primer coatings, Prog. Org. Coat. 77 (2014) 1946–1956.

[9] S. Sellaiyan, A.E. Hughes, S.V. Smith, A. Uedono, J. Sullivan, S. Buckman, Leaching properties of chromate-containing epoxy films using radiotracers, PALS and SEM, Prog. Org. Coat. 77 (2014) 257–267.

[10] M.W. Kendig, R.G. Buchheit, Corrosion inhibition of aluminum and aluminum alloys by soluble chromates, chromate coatings, and chromate-free coatings, Corrosion 59 (2003) 379–400.

[11] B. Kannan, C.F. Glover, H.N. McMurray, G. Williams, J.R. Scully, Performance of a magnesium-rich primer on pretreated AA2024-T351 in full immersion: a galvanic throwing power investigation using a scanning vibrating electrode technique, J. Electrochem. Soc. 165 (2018) C27–C41.

[12] J.R. Scully, F. Presuel-Moreno, M. Goldman, R.G. Kelly, N. Tailleart, User-selectable barrier, sacrificial anode, and active corrosion inhibiting properties of Al-Co-Ce alloys for coating applications, Corrosion 64 (2008) 210–229.

[13] J.R. Scully, N. Tailleart, F. Presuel-Moreno, 9 – Tunable multifunctional corrosion-resistant metallic coatings containing rare earth elements, Rare Earth-Based Corrosion Inhibitors, Woodhead Publishing, 2014, pp. 267–290.

[14] F.J. Presuel-Moreno, H. Wang, M.A. Jakab, R.G. Kelly, J.R. Scully, Computational modeling of active corrosion inhibitor release from an Al-Co-Ce metallic coating – protection of exposed AA2024-T3, J. Electrochem. Soc. 153 (2006) B486–B498.

[15] P. Visser, H. Terryn, J.M.C. Mol, On the importance of irreversibility of corrosion inhibitors for active coating protection of AA2024-T3, Corros. Sci. 140 (2018) 272–285.

[16] P. Visser, S.A. Hayes, Low-temperature-curable coating composition useful as anticorrosive primer coating for non-ferrous metal substrates, particularly aluminum or aluminum alloy, comprises film-forming resin, curing agent, and lithium salt, patent nr. WO2010112605-A1, (2010).

[17] O. Gharbi, S. Thomas, C. Smith, N. Birbilis, Chromate replacement: what does the future hold? npj Mater. Degrad. 2 (2018) 12.

[18] P. Visser, Y. Liu, H. Terryn, J.M.C. Mol, Lithium salts as leachable corrosion inhibitors and potential replacement for hexavalent chromium in organic coatings for the protection of aluminum alloys, J. Coat. Technol. Res. 13 (2016) 557–566.

[19] P. Visser, H. Terryn, J.M.C. Mol, On the importance of irreversibility of corrosion inhibitors for active coating protection of AA2024-T3, Corros. Sci. 140 (2018) 272–285.

[20] P. Visser, Y. Liu, X. Zhou, T. Hashimoto, G.E. Thompson, S.B. Lyon, L.G.J. van der Ven, A.J.M.C. Mol, H.A. Terryn, The corrosion protection of AA2024-T3 aluminium alloy by leaching of lithium-containing salts from organic coatings, Faraday Discuss. 180 (2015) 511–526.

[21] P. Visser, A. Lutz, J.M.C. Mol, H. Terryn, Study of the formation of a protective layer in a defect from lithium-leaching organic coatings, Prog. Org. Coat. 99 (2016) 80–90.

[22] P. Visser, M. Meeusen, Y. Gonzalez-Garcia, H. Terryn, J.M.C. Mol, Electrochemical evaluation of corrosion inhibiting layers formed in a defect from lithium-leaching organic coatings, J. Electrochem. Soc. 164 (2017) C396–C406.

[23] Y. Liu, P. Visser, X. Zhou, S.B. Lyon, T. Hashimoto, M. Curioni, A. Gholinia, G.E. Thompson, G. Smyth, S.R. Gibbon, D. Graham, J.M.C. Mol, H. Terryn, Protective film formation on AA2024-T3 aluminum alloy by leaching of lithium carbonate from an organic coating, J. Electrochem. Soc. 163 (2016) C45–C53.

[24] Y. Liu, P. Visser, X. Zhou, S.B. Lyon, T. Hashimoto, A. Gholinia, G.E. Thompson, G. Smyth, S.R. Gibbon, D. Graham, J.M.C. Mol, H. Terryn, An investigation of the corrosion inhibitive layers generated from lithium oxalate-containing organic coating on AA2024-T3 aluminium alloy, Surf. Interface Anal. 48 (2016) 798–803.

[25] K. Marcoen, P. Visser, G.F. Trindade, M.L. Abel, J.F. Watts, J.M.C. Mol, H. Terryn, T. Hauffman, Compositional study of a corrosion protective layer formed by leachable lithium salts in a coating defect on AA2024-T3 aluminium alloys, Prog. Org. Coat. 119 (2018) 65–75.

[26] J.D. Gorman, A.E. Hughes, D. Jamieson, P.J.K. Paterson, Oxide formation on aluminium alloys in boiling deionised water and NaCl, CeCl3 and CrCl3 solutions, Corros. Sci. 45 (2003) 1103–1124.

[27] R.G. Buchheit, M.D. Bode, G.E. Stoner, Corrosion-resistant, chromate free talc coatings for aluminum, Corrosion 50 (1994) 205–214.

[28] G.F. Trindade, J. Bañuls-Ciscar, C.K. Ezeh, M.L. Abel, J.F. Watts, Characterisation of wood growth regions by multivariate analysis of ToF-SIMS data, Surf. Interface Anal. 48 (2016) 584–588.

[29] G.F. Trindade, M.-L. Abel, J.F. Watts, simsMVA: a tool for multivariate analysis of ToF-SIMS datasets, Chemom. Intell. Lab. Syst. 182 (2018) 180–187.

[30] G.F. Trindade, M.-L. Abel, C. Lowe, R. Tshulu, J.F. Watts, A time-of-flight secondary ion mass spectrometry/multivariate analysis (ToF-SIMS/MVA) approach to identify phase segregation in blends of incompatible but extremely similar resins, Anal. Chem. 90 (2018) 3936–3941.

[31] M.R. Keenan, P.G. Kotula, Accounting for poisson noise in the multivariate analysis of ToF-SIMS spectrum images, Surf. Interface Anal. 36 (2004) 203–212.

[32] G.F. Trindade, M.-L. Abel, J.F. Watts, Non-negative matrix factorisation of large mass spectrometry datasets, Chemom. Intell. Lab. Syst. 163 (2017) 76–85.

[33] D.D. Lee, H.S. Seung, Learning the parts of objects by non-negative matrix factorization, Nature 401 (1999) 788.

[34] A. Seidell, Solubilities of Inorganic and Organic Compounds c. 2, D. Van Nostrand Company, 1919.

[35] R.C. Weast, CRC Handbook of Chemistry and Physics, 1st student edition, CRC Press, Boca Raton, 1988.

[36] H. Terryn, J. Vereecken, G.E. Thompson, The electrograining of aluminium in hydrochloric acid—II. Formation of ETCH products, Corros. Sci. 32 (1991) 1173–1188.

[37] S. Van Gils, C.A. Melendres, H. Terryn, Quantitative chemical composition of thin films with infrared spectroscopic ellipsometry: application to hydrated oxide films on aluminium, Surf. Interface Anal. 35 (2003) 387–394.

[38] S. Van Gils, P. Mast, E. Stijns, H. Terryn, Colour properties of barrier anodic oxide films on aluminium and titanium studied with total reflectance and spectroscopic ellipsometry, Surf. Coat. Technol. 185 (2004) 303–310.

[39] P. Visser, Y. Gonzalez-Garcia, J.M.C. Mol, H. Terryn, Mechanism of passive layer formation on AA2024-T3 from alkaline lithium carbonate solutions in the presence of sodium chloride, J. Electrochem. Soc. 165 (2018) C60–C70.

[40] P. Visser, Novel totally chrome free corrosion inhibiting coating technology for protection of aluminium alloys, Trans. Inst. Met. Finish. 89 (2011) 291–294.

[41] L. Van Vaeck, Molecular speciation analysis of inorganic compounds, in: J.C. Vickerman (Ed.), ToF-SIMS : Material Analysis by Mass Spectrometry, 2013, pp. 125–150 Chichester: IM.

[42] R.T. Foley, Localized corrosion of aluminum alloys – a review, Corrosion 42 (1986) 277–288.

[43] R.T. Foley, T.H. Nguyen, The chemical nature of aluminum corrosion: V. Energy transfer in aluminum dissolution, J. Electrochem. Soc. 129 (1982) 464–467.

[44] R.S. Alwitt, The growth of hydrous oxide films on aluminum, J. Electrochem. Soc. 121 (1974) 1322–1328.

[45] L.A. Carreiea, V.A. Maroni, J.W. Swaine Jr, R.C. Plumb, Raman and infrared spectra and structures of the aluminate ions, J. Chem. Phys. 45 (1966) 2216–2220.

[46] M.R. Tabrizi, S.B. Lyon, G.E. Thompson, J.M. Ferguson, The long-term corrosion of aluminium in alkaline media, Corros. Sci. 32 (1991) 733–742.

[47] C.A. Drewien, M.O. Eatough, D.R. Tallant, C.R. Hills, R.G. Buchheit, Lithium-aluminum-carbonate-hydroxide hydrate coatings on aluminum: composition, structure and processing bath chemistry, J. Mater. Res. 11 (1996) 1507–1513.

[48] W. Vedder, D.A. Vermilyea, Aluminum + water reaction, Trans. Faraday Soc. 65 (1969) 561–584.